

# On the spin-temperature evolution during the epoch of reionization

Rajat M. Thomas<sup>1,2,3\*</sup>, Saleem Zaroubi<sup>1,4</sup>

<sup>1</sup>*Kapteyn Astronomical Institute, University of Groningen, P.O. Box 800, 9700 AV Groningen, the Netherlands.*

<sup>2</sup>*Institute for the Mathematics and Physics of the Universe (IPMU), The University of Tokyo, Chiba, 277-8582, Japan.*

<sup>3</sup>*CITA, University of Toronto, 60. St. George Street, M5S 3H8, Toronto, ON, Canada.*

<sup>4</sup>*Physics Department, Technion, Haifa 32000, Israel.*

## ABSTRACT

Simulations estimating the brightness temperature ( $\delta T_b$ ) of the redshifted 21-cm from the epoch of reionization (EoR) often assume that the spin temperature ( $T_s$ ) is decoupled from the background CMB temperature and is much larger than it, i.e.,  $T_s \gg T_{\text{CMB}}$ . Although a valid assumption towards the latter stages of the reionization process, it does not necessarily hold at the earlier epochs. Violation of this assumption will lead to fluctuations in  $\delta T_b$  that are neither driven by density fluctuations nor by  $\text{H II}$  regions. Therefore, it is vital to calculate the spin temperature self-consistently by treating the  $\text{Ly}\alpha$  and collisional coupling of  $T_s$  to the kinetic temperature,  $T_k$ . In this paper we develop an extension to the BEARS algorithm, originally developed to model reionization history, to include these coupling effects. Here we simulate the effect in ionization and heating for three models in which the reionization is driven by stars, miniquasars or a mixture of both. We also perform a number of statistical tests to quantify the imprint of the self-consistent inclusion of the spin temperature decoupling from the CMB. We find that the evolution of the spin temperature has an impact on the measured signal specially at redshifts higher than 10 and such evolution should be taken into account when one attempts to interpret the observational data.

**Key words:** Physical data processes: radiative transfer – cosmology: theory – observation – diffuse radiation – radio lines: general.

## 1 INTRODUCTION

Physical processes that occur during reionization are numerous and complex. Nevertheless, ionization of neutral gas (hydrogen & helium) and heating of the inter-galactic medium (IGM) can be considered the two primary influences of radiating objects during reionization.

Currently, the most promising “direct” probe of reionization is the redshifted 21-cm radiation emanating from neutral hydrogen during the epoch of reionization (EoR), which are to be measured using upcoming telescopes like LOFAR<sup>1,2</sup>, MWA<sup>3</sup>, PAPER<sup>4</sup> and 21CMA<sup>5</sup>. The intensity of the observed 21-cm radiation depends on the ratio between the number density of electrons in the hyperfine states in the ground state of a neutral hydrogen atom. This ratio is normally expressed in terms of the so-called 21-cm spin temperature,  $T_s$ . At the onset of the formation of the first reionizing objects the spin temperature is equal to the CMB temperature since

at these redshifts the ratio between excited and ground hyperfine state electrons is completely determined by the CMB. However, as the number of ionizing sources increases,  $T_s$  starts departing from  $T_{\text{CMB}}$ ; slowly at the beginning, then rapidly approaching values larger than  $T_{\text{CMB}}$ . This evolution is typically ignored in most previous studies of reionization which assumes  $T_s \gg T_{\text{CMB}}$  at all times (Mellema et al. 2006; Abel & Norman 2000, 2002; Bromm et al. 2002; Yoshida et al. 2003).

Recently, Baek et al. (2009) have relaxed this assumption on  $T_s$  at the dawn of reionization and explored its impact on the brightness temperature. They found a considerable deviation from assuming  $T_s \gg T_{\text{CMB}}$  at the beginning of reionization. Towards the end of reionization though, this assumption holds ground. But, in order to track the evolution of  $T_s$  accurately, like in Baek et al. (2009), it is necessary to perform a detailed 3-D  $\text{Ly}\alpha$  radiative transfer calculation. The  $\text{Ly}\alpha$  photons undergo a large number ( $\sim 10^5$ ) of scatterings even in a marginally neutral medium before it is sufficiently off line-centre to “free stream”. The scattering angle after each encounter is completely random and therefore the radiative transfer is often done in a Monte Carlo sense (Tasitomi 2006; Baek et al. 2009; Pierleoni et al. 2009; Laursen et al. 2009) to capture this random nature of  $\text{Ly}\alpha$  scatterings.

Unfortunately these Monte Carlo radiative transfer schemes are computationally very expensive, especially if we need to sim-

\* E-mail: thomas@cita.utoronto.ca

<sup>1</sup> [www.lofar.org](http://www.lofar.org)

<sup>2</sup> [www.astro.rug.nl/~LofarEoR](http://www.astro.rug.nl/~LofarEoR)

<sup>3</sup> <http://www.mwatelescope.org/>

<sup>4</sup> <http://astro.berkeley.edu/~dbacker/eor/>

<sup>5</sup> <http://21cma.bao.ac.cn/>

ulate large fields of view necessary to generate mock data sets for next generation radio telescopes. In order to circumvent the need to perform such computer-intensive calculations to obtain  $T_s$ , we develop an algorithm along the lines of BEARS (Thomas et al. 2009) as an approximation. In this paper we present an algorithm that follows the decoupling of  $T_s$  from  $T_{\text{CMB}}$  owing to  $\text{Ly}\alpha$  photons, which couples the spin temperature to the colour/kinetic temperature via the Wouthuysen-Field effect (Wouthuysen 1952). Collisional excitation and heating caused by secondary electrons resulting from hard X-ray radiation are also included. The dominant source of  $\text{Ly}\alpha$  flux is the background created by the redshifting of photons in the Lyman band into  $\text{Ly}\alpha$ . These photons are blueward of  $\text{Ly}\alpha$  and is injected into  $\text{Ly}\alpha$  at some distance away from the source.

The amount of intrinsic  $\text{Ly}\alpha$ , ionizing and “heating” photons is a function of the source spectral energy distribution (SED). Thus the evolution of the spin temperature critically depends on the source of reionization. Different reionization sources manifest themselves by influencing the IGM in markedly different ways. For example, deficiency of hard photons in the SEDs of “first stars”, limit the extent to which they heat the IGM (Thomas & Zaroubi 2008; Zaroubi et al. 2007; Zaroubi & Silk 2005), while miniquasars (or miniqsos, characterized by central black hole masses less than a million solar), abundant in X-ray photons, cause considerable heating (Madau, Meiksin, & Rees 1997; Ricotti & Ostriker 2004; Nusser 2005; Furlanetto, Zaldarriaga, & Hernquist 2004; Wyithe & Loeb 2004; Furlanetto & Loeb 2002; Thomas & Zaroubi 2008; Zaroubi et al. 2007). Ionization profiles similarly have their characteristic source-dependent behavior.

Although the question on which sources did the bulk of the reionization is up for debate, it is conceivable from observations of the local Universe up to redshifts around 6.5, that sources of reionization could have been a mixture of both stellar and quasar kinds (their respective roles again are uncertain). Implementing radiative transfer that include both ionizing and hard X-ray photons has been difficult and as a result most 3-D radiative transfer schemes restrict themselves to ionization due to stars (Gnedin & Abel 2001; Ciardi et al. 2001; Ritzerveld, Icke, & Rijkhorst 2003; Susa 2006; Razoumov & Cardall 2005; Nakamoto, Umemura, & Susa 2001; Whalen & Norman 2006; Rijkhorst et al. 2006; Mellema et al. 2006; Zahn et al. 2007; Mesinger & Furlanetto 2007; Pawlik & Schaye 2008). In Ricotti & Ostriker (2004), a “semi” hybrid model of stars and miniqsos, like the one hinted above, has been used albeit in sequential order instead of a simultaneous implementation. That is, pre-ionization due to miniqsos was invoked between  $7 \leq z \leq 20$ , after which, stars reionize the Universe at redshift 7. We in this paper would like to address the issue of simulating the propagation of both the UV and hard X-ray photons, exactly in 1-D and as approximation in 3-D.

The focus of this paper is therefore to introduce the algorithm that is used to implement IGM heating in BEARS along with the procedure to estimate the spin temperature of the IGM. As an application of this technique we explore the effects of heating due to miniqsos, stars and, for the first time, a mixed “hybrid population”. Subsequently, we provide quantitative and qualitative analysis of the differences in the 21-cm EoR signal with and without the usual assumption of  $T_s$  being always decoupled from  $T_{\text{CMB}}$ .

The paper is organized as follows; §2 describes briefly the N-body and 1-D radiative transfer codes used. In §3 we describe the adaptation of BEARS to include  $T_k$ , followed by the calculation of the  $T_s$  and  $\delta T_b$  within the simulation box. BEARS is then applied to three different scenarios of reionization in §4, *viz.*, (1) the primary

source being stars, (2) miniqsos and (3) a hybrid population of stars and miniqsos. Subsequently, observational cubes of  $\delta T_b$  are generated for each of these scenarios and its properties discussed. In §5 we provide statistics on the simulated boxes and interpret the finding mainly from the point of view of the differences in  $\delta T_b$  with and without the usual assumption that  $T_s$  is decoupled from  $T_{\text{CMB}}$ . We also compare our work to that of Santos et al. (2008) in the same section. Conclusions and discussions of the results are presented in §6, along with a mention of a few topics that can be addressed using the data set simulated in this paper.

## 2 SIMULATIONS

In this section we briefly mention the dark-matter-only N-body simulations employed, the 1-D radiative transfer code developed by Thomas & Zaroubi (2008) and provide an overview of the BEARS algorithm designed in Thomas et al. (2009).

### 2.1 N-body: dark matter only

The dark matter only N-body simulations are the same as in Thomas et al. (2009) and was performed by Joop Schaye and Andreas Pawlik at the Leiden observatory. The N-body/TreePM/SPH code GADGET (Springel 2005) was used to perform a dark matter (DM) cosmological simulation containing  $512^3$  particles in a box of size  $100 h^{-1}$  comoving Mpc with each DM particle having a mass of  $4.9 \times 10^8 h^{-1} M_\odot$ .

Initial conditions for the particle’s position and velocity were obtained from glass-like initial conditions using CMBFAST (version 4.1; Seljak & Zaldarriaga (1996)) and the Zelovich approximation was used to linearly evolve the particles down to redshift  $z = 127$ . A flat  $\Lambda$ CDM universe is assumed with the set of cosmological parameters  $\Omega_m = 0.238$ ,  $\Omega_b = 0.0418$ ,  $\Omega_\Lambda = 0.762$ ,  $\sigma_8 = 0.74$ ,  $n_s = 0.951$  and  $h = 0.73$  (Spergel et al. 2007). Snapshots were written out at 35 equally spaced redshifts between  $z = 12$  and  $z = 6$ . Halos were identified using the Friends-of-Friends algorithm (Davis et al. 1985), with linking length  $b = 0.2$ . The smallest mass haloes we can resolve are a few times  $10^{10} h^{-1} M_\odot$ . The density field was smoothed on the mesh with a Gaussian kernel with standard deviation  $\sigma_G = 2 \times 100/512$  comoving Mpc/ $h$  (2 grid cells).

### 2.2 1-D radiative transfer (RT) code.

The implementation of the 1-D radiative transfer code is modular and hence straightforward to include different spectra corresponding to different ionizing sources. Our 1-D code can handle X-ray photons, the secondary ionization and heating it causes, and as a result perform well both for high (quasars/miniqsos) and low energy (stars) photons. Further details of the code can be found in Thomas & Zaroubi (2008).

The parameter space simulated by the 1-D radiative transfer scheme (Thomas & Zaroubi 2008) include; 1) different SEDs (stars or miniqsos with different power-law indices), 2) duration of evolution (depending on the life-time of the source), 3) redshifts at which these sources turn on and 4) clumping factor or over-density around a given source. Information on the ionization and temperature profiles from these simulations were cataloged to be used later as in Thomas et al. (2009). Density profiles around sources are assumed to be homogeneous although the code could be initialized using any given profile.

### 2.3 BEARS algorithm: overview

BEARS is a fast algorithm that simulates the underlying cosmological 21-cm signal from the EoR. It is implemented by using the Nbody/SPH simulation in conjunction with a 1-D radiative transfer code; both discussed in the previous sections. The basic steps of the algorithm are as follows: first, a catalogue of 1-D ionization profiles of all atomic hydrogen and helium species and the temperature profile that surround the source is calculated for different types of ionizing sources with varying masses, luminosities at different redshifts. Subsequently, photon rates emanating from dark matter haloes, identified in the N-body simulation, are calculated semi-analytically. Finally, given the spectrum, luminosity and the density around the source, a spherical ionization bubble is embedded around the source, whose radial profile is selected from the catalogue as generated above. In case of overlap between ionization bubbles, the excess ionized atoms in the overlap area is redistributed at the edge of the bubbles. For more details see Thomas et al. (2009). The outputs are data cubes (2-D slices along the frequency/redshift direction) of density ( $\delta$ ), radial velocity ( $v_r$ ) and hydrogen and helium fractions ( $x_{\text{HI, HII, HeI, HeII\&HeIII}}$ ). Each data cube consists of a large number of slices each representing a certain redshift between 6 and 11.5. Because these slices are produced to simulate a mock dataset for radio-interferometric experiments, they are uniformly spaced in frequency (therefore, not uniform in redshift). Thus, the frequency resolution of the instrument dictates the scales over which structures in the Universe are averaged/smoothed along the redshift direction. The relation between frequency and redshift space  $z$  is given by:  $z = \frac{\nu_{21}}{\nu} - 1$ , where  $\nu_{21} = 1420$  MHz is the rest frequency that corresponds to the 21-cm line.

## 3 INCLUDING IGM HEATING IN BEARS

In Thomas et al. (2009) the BEARS algorithm was introduced; a special-purpose 3-D radiative transfer scheme used to simulate cosmological EoR signals. In that paper we detailed the philosophy behind the code and its implementation to incorporate ionization due to a variety of sources. In this section, we extend the features of BEARS to include heating (on which the brightness temperature is sensitively dependent) due to hard photons within the same framework.

The algorithm to implement heating begins in a manner similar to that for ionization. The  $T_k$ -profile from the 1-D radiative transfer code is used to embed a spherically symmetric “ $T_k$  bubble” at the locations of the centre-of-mass of dark matter haloes. The luminosity of the source is a function of the halo mass. The problem embedding a temperature profile in the simulation box is that, the radius of the bubble is large ( $> 5$  Mpc) and results in extensive overlap, even at high redshifts; a problem encountered for ionization bubbles only towards the end of reionization. In a quasar dominated part of the Universe this is particularly severe because of its large sphere-of-influence in heating the IGM.

### 3.1 Treating overlaps: Energy conservation

Overlap in the spheres of ionized regions was treated by redistributing the excess ionizing photons in the overlapped region uniformly around the overlapping spheres (Thomas et al. 2009). Treating overlapped zones directly in terms of temperatures makes it difficult to come up with any “conserved quantity”. To elaborate, consider a pre-ionized zone in the simulation box close to the radiating

source. Although at close proximity to the source, this region is not heated efficiently because of the absence of neutral hydrogen to capture the photons. On the other hand, the same source can dump more energy into an initially neutral zone that maybe far away from it. Thus, embedding the  $T_k$ -profile directly from the catalog (which assumes uniform IGM density) is not appropriate.

Here we adopt a different approach where we estimate the total energy deposited in every region of the simulation box and invoke the conservation of energy deposited by the sources in the overlapped regions. We integrate the contribution to the energy budget, at a given location, from all sources whose sphere-of-influence extends to that location. This total energy is then redistributed equally to all the contributing sources, i.e., the energy output of each source is modified to account for the overlapping.

To illustrate, consider  $\mathcal{N}$  sources that overlap at a particular location  $\vec{r}$  and the total energy estimated at that location to be  $E_{tot} = \sum_{i=1}^{\mathcal{N}} E_i$ , where  $E_i$  is the energy deposited by the  $i^{th}$  source at location  $\vec{r}$ . The fraction of “excess” energy attributed to each of the  $\mathcal{N}$  sources is  $\delta E = E_{tot}/\mathcal{N}$ . This energy  $\delta E$  is then added to the total energy from the source to estimate a new normalization constant for the SED of the source. For example in case of a power-law-type source, the SED includes a normalization term that is determined by the total energy of the source,  $E_{total}$ . However, in the overlap case the total energy of the source is replaced by  $E_{total} + \delta E$ . Now a “new” bubble of kinetic temperature is embedded whose profile depends on a source whose output energy has gotten a  $\delta E$  boost. In this manner  $T_k(\vec{r})$  is estimated at every location in the simulation box. From this point on we need to estimate the coefficients that couple  $T_k$  to  $T_s$  that will eventually lead to the estimation of  $\delta T_b$ . It is worthwhile also to note that the results are robust to variation in the exact algorithm used to treat the overlapped region. For example, if we choose to sum the energies deposited directly in a given region or choose  $\max(E_1, E_2, \dots, E_n)$ , where  $E_1 \dots E_n$  are energies deposited by sources 1...n respectively, the final results are very similar.

This is obviously an approximation which assumes that the efficiency of the photons in heating the IGM does not depend on their frequency. For the case of power-law sources where most of the energy comes from hard photons this is probably a reasonable approximation. However, in the case of blackbody sources this is not a very good assumption because evidently the heating is done by a very small fraction of photons. But in these cases the overlap problem is not as severe as for the power-law sources since the extent of the heating is much more limited. In summary, despite the approximate nature of this approach, it provides an efficient and reasonable resolution for the issue of the overlapping of temperature bubbles. We note that self consistent treatment of this problem requires taking into account the modification of each of sources’ SED in a different manner depending on the amplitude of its SED. Obviously this is computationally very expensive.

### 3.2 Calculating $\delta T_b$ in the volume

Spin temperature can be thought of as a short hand notation to represent the level population of the hyperfine states of the ground level of a hydrogen atom. Depending on the physical processes and background radiation that dominate a medium,  $T_s$  is either coupled to the background CMB temperature or to the kinetic temperature of the hydrogen gas in the medium. Formally Field (1958) derived  $T_s$  as a weighted sum of  $T_k$  and  $T_{\text{CMB}}$ , as;

$$T_s^{-1} = \frac{T_{\text{CMB}}^{-1}(z) + y_\alpha T_k^{-1} + y_{\text{coll}} T_k^{-1}}{1 + y_\alpha + y_{\text{coll}}}, \quad (1)$$

where  $y_\alpha$  and  $y_{\text{coll}}$  are parameters that reflect the coupling of  $T_s$  to  $T_k$  via  $\text{Ly}\alpha$  excitation and collisions respectively. The efficiency of  $\text{Ly}\alpha$ -coupling dominates over that of collisions, especially further away from the source (Thomas & Zaroubi 2008; Chuzhoy, Alvarez, & Shapiro 2006). In our treatment of calculating  $T_s$ , we estimate both  $y_\alpha$  and  $y_{\text{coll}}$ .

The coefficient  $y_{\text{coll}}$  is a function of  $T_k$  and the ionization fraction of the medium,  $x_{\text{HII}}$ . These informations on ionization and heating are available from the prescription outlined in the previous section. While simulating the 1-D profiles we simultaneously calculate  $y_\alpha$  as;

$$y_\alpha = \frac{16\pi^2 T_* e^2 f_{12} J_o(|r|)}{27 A_{10} T_e m_e c}. \quad (2)$$

Here,  $J_o(|r|)$  is the  $\text{Ly}\alpha$  flux density at distance  $r$  from the source. For miniquas with high energy photons,  $\text{Ly}\alpha$  coupling is mainly caused by collisional excitation due to secondary electrons (Chuzhoy, Alvarez, & Shapiro 2006). This process is accounted for by the following integral,

$$J_o(|r|) = \frac{c}{4\pi H(z)\nu_\alpha} n_{\text{HI}}(r) \int_{50\text{eV}}^{2\text{KeV}} \phi_\alpha(E) \sigma(E) N(E; r, t) dE, \quad (3)$$

where  $N(E; r; t)$  is the number of photons with energy 'E' at radius 'r', and time 't' per unit area (Zaroubi & Silk 2005). This number is obtained directly from the 1-D radiative transfer by taking into account the the absorption due to the optical depth along the line-of-sight to the source at a distance 'r'. The 1-D profiles generated are catalogued also as a function of time. Therefore the profiles that are embedded within the simulation are chosen to obey causality<sup>6</sup>. The ionization cross-section of neutral hydrogen in the ground state is given by  $\sigma(E)$ ,  $f_{12} = 0.416$  is the oscillator strength of the  $\text{Ly}\alpha$  transition,  $e$  &  $m_e$  are the electron's charge and mass, respectively,  $\phi_\alpha$  is the fraction of the absorbed photon energy that goes into excitation (Shull & van Steenberg 1985; Dijkstra, Haiman, & Loeb 2004). Note here that the fitting formula is a function of both ionization fraction and energy as given in the appendix of Dijkstra, Haiman, & Loeb (2004).

For the case of stars, the dominant source of  $\text{Ly}\alpha$  flux results from the redshifting of the source spectrum blueward of  $\text{Ly}\alpha$  into the resonant line at different distances from the source. Frequency ' $\nu$ ' at the redshift of emission (or the source) ' $z$ ' is redshifted into  $\nu_{L\text{Ly}\alpha}$  at redshift  $z(|r|)$  such that;

$$\nu = \nu_{L\text{Ly}\alpha} \frac{1+z}{1+z(|r|)}. \quad (4)$$

Thus, at every radius  $r$  away from the source the  $\text{Ly}\alpha$  flux  $J_o(|r|) \propto N(E'; r; t)/r^2$ . Where  $E' = 10.2 \frac{1+z}{1+z(|r|)}$  [eV].

Now, instead of embedding a sphere of the  $T_s$ , as in the case of  $T_k$ , we embed instead the a bubble of  $\text{Ly}\alpha$  flux,  $J_o(|r|)$ , as estimated from Eq. 3. Since  $J_o(|r|)$  is basically the number of  $\text{Ly}\alpha$  photons at a given location, the overlap of two "J<sub>o</sub> bubbles" implies that the photons and hence the J<sub>o</sub> has to be added, i.e., at a given spatial (pixel) location,  $\vec{x}$ ,  $\vec{y}$ ,  $\vec{z}$  and time  $t$ , the total  $\text{Ly}\alpha$  flux is given by;

$$J_o^{\text{tot}}(\vec{x}, \vec{y}, \vec{z}, t) = \sum_{i=0}^N J_o^i(\vec{x}, \vec{y}, \vec{z}, t), \quad (5)$$

where  $J_o^i(\vec{x}, \vec{y}, \vec{z}, t)$  is the  $\text{Ly}\alpha$  flux contributed by  $i^{\text{th}}$  source at the pixel location in the box,  $\vec{x}$ ,  $\vec{y}$ ,  $\vec{z}$  and time  $t$ . Equipped with the quantities  $T_k(\vec{r})$ , and  $J_o(\vec{r})$ , we can calculate  $y_\alpha$  as in Eq. 2, and subsequently the spin temperature through Eq. 1. Now all terms required for the calculation of  $\delta T_b$ , as in Eq. 6, are obtained.

$$\delta T_b(\vec{r}) = (20 \text{ mK}) (1 + \delta(\vec{r})) \left( \frac{x_{\text{HI}}(\vec{r})}{h} \right) \left( 1 - \frac{T_{\text{CMB}}}{T_s(\vec{r})} \right) \times \left[ \frac{H(z)/1+z}{dv_{\parallel}/dr_{\parallel}} \right] \left( \frac{\Omega_b h^2}{0.0223} \right) \left[ \left( \frac{1+z}{10} \right) \left( \frac{0.24}{\Omega_m} \right) \right]^{1/2} \quad (6)$$

## 4 EXAMPLE APPLICATIONS OF BEARS

In this section we apply BEARS with its extended feature of including heating of the IGM, to three different scenarios of reionization. The models described in this section are not "template" reionization scenarios by any measure nor is any particular model favoured w.r.t the other. In fact, these models may be far from reality and only serve as examples of the potential of BEARS to provide a reasonable estimate of the 21-cm brightness temperature for widely different scenarios of reionization.

### 4.1 Heating due to stars

The first scenario explored using BEARS is the case in which the sources of reionization are *only* stars. In this section we describe the model used to describe the stellar component and the prescription adopted to embed these stars into haloes of dark matter identified in an N-body simulation.

#### 4.1.1 Modeling stellar radiation in BEARS

Most stars, to first order, behave as blackbodies at a given temperature, although the detailed features in the SED depends on more complex physical processes, age, metallicity and mass of the star. This blackbody nature imprints characteristic signatures on the IGM heating and ionization patterns (Thomas & Zaroubi 2008). Schaerer (2002) showed that the temperature of the star only weakly depends on its mass. The blackbody temperature of the stars in our simulation was thus fixed at  $5 \times 10^4$  K to perform the radiative transfer. We sample the parametre space of redshifts (12 to 6), density profiles around the source<sup>7</sup> and masses (10 to 1000  $M_\odot$ ). The total luminosity is normalized depending on the mass of the star according to Table. 3 in Schaerer (2002).

For blackbody with a temperature around  $10^5$  K, similar to our adopted value, the spectrum peaks between  $\approx 20$  eV to  $\approx 24$  eV (Wien's displacement law). Thus, from the form of the blackbody spectrum we can apriori expect, in the case of stars, that the ionization induced by these objects will be high, but the heating they cause will not be substantial given the exponential cutoff of the radiation towards higher frequencies.

<sup>6</sup> Of course the catalogue has been generated with a a particular time resolution and can be made finer for more accurate results

<sup>7</sup> We can incorporate any given density profile like the homogeneous, isothermal or NFW profiles. For this paper however we ran all the simulations using a homogeneous background. Overdensities around sources can be corrected for by using the prescription in Thomas et al. (2009).

Now, following the prescription in Thomas et al. (2009) we associate stellar spectra with dark matter halos using the following procedure. The global star formation rate density  $\dot{\rho}_*(z)$  as a function of redshift was calculated using the empirical fit;

$$\dot{\rho}_*(z) = \dot{\rho}_m \frac{\beta \exp[\alpha(z - z_m)]}{\beta - \alpha + \alpha \exp[\beta(z - z_m)]} [\text{M}_\odot \text{ yr}^{-1} \text{ Mpc}^{-3}], \quad (7)$$

where  $\alpha = 3/5$ ,  $\beta = 14/15$ ,  $z_m = 5.4$  marks a break redshift, and  $\dot{\rho}_m = 0.15[\text{M}_\odot \text{ yr}^{-1} \text{ Mpc}^{-3}]$  fixes the overall normalisation (Springel & Hernquist 2003). Now, if  $\delta t$  is the time-interval between two outputs in years, the total mass density of stars formed is

$$\rho_*(z) \approx \dot{\rho}_*(z) \delta t [\text{M}_\odot \text{ Mpc}^{-3}]. \quad (8)$$

Notice that this approximation is valid only if the typical lifetime of the star is much smaller than  $\delta t$ , which indeed is the case in our model because the stellar mass we input ( $100 \text{ M}_\odot$ ) has a lifetime of about a few Myrs (Schaerer 2002), compared to a typical time difference of few tens of Myrs between simulation snapshots.

Therefore, the total mass in stars within the simulation box is  $M_*(\text{box}) \approx L_{\text{box}}^3 \rho_*$  [ $\text{M}_\odot$ ]. This mass in stars is then distributed among the halos weighted by their mass;

$$m_*(\text{halo}) = \frac{m_{\text{halo}}}{M_{\text{halo}}(\text{tot})} M_*(\text{box}), \quad (9)$$

where  $m_*(\text{halo})$  is the mass in stars in the dark matter ‘‘halo’’,  $m_{\text{halo}}$  the mass of the halo and  $M_{\text{halo}}(\text{tot})$  the total mass in halos within the simulation box.

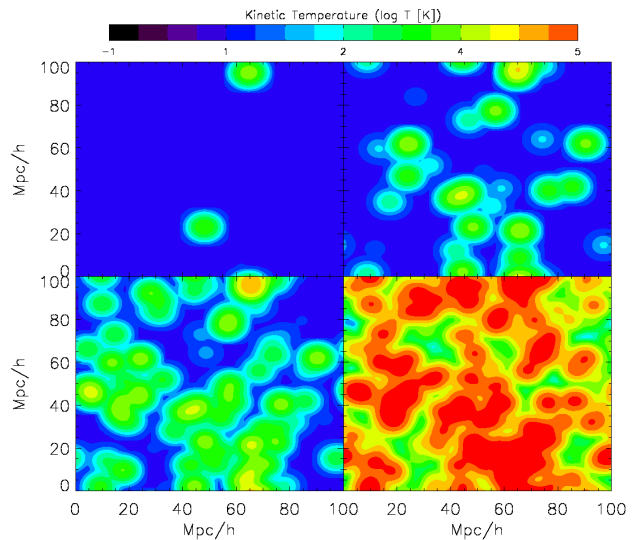
We then assume that all of the mass in stars is distributed in stars of  $100 \text{ M}_\odot$ , which implies that the number of stars in the halo is  $N_{100} = 10^{-2} \times m_*(\text{halo})$ . The luminosity of a  $100 \text{ M}_\odot$  star is obtained from Fig. 1 of Schaerer (2002), assuming zero metallicity. The luminosity of  $100 \text{ M}_\odot$  star thus derived is in the range of  $10^6 - 10^7 L_\odot$  and this value is multiplied by  $N_{100}$  to get the total luminosity emanating from the ‘‘halo’’ and the radiative transfer is done by normalizing the blackbody spectrum to this value. The escape fractions of ionizing photons from early galaxies is assumed to be 10%.

#### 4.1.2 Results: Stellar sources

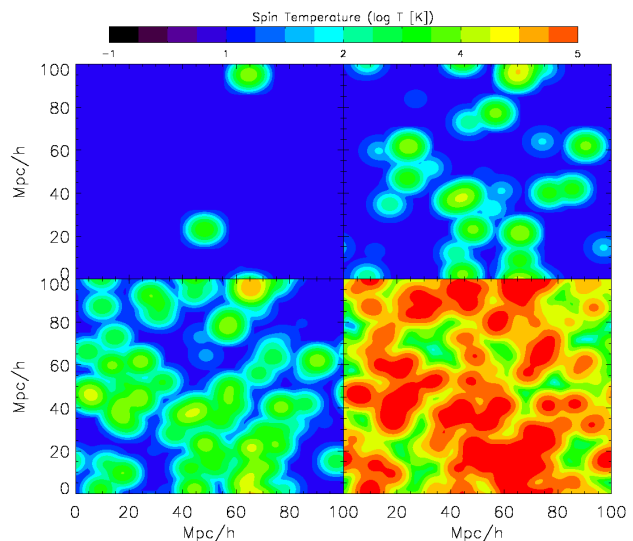
Results of the evolution of the  $T_k$ ,  $T_s$  and  $\delta T_b$  of the IGM, when the sources of reionization comprise only of stars is shown in Figs 1, 2 and 3, respectively.

Figure 1 shows the kinetic temperature for stellar sources at redshifts 10, 8, 7 and 6 at which their ionized fractions are 0.12, 0.5, 0.83, and 0.98 respectively. The blackbody type stellar spectra do not have sufficient high energy photons to heat the IGM substantially far away from the source. Thus we see compact regions (bubbles) of high temperature in the immediate vicinity of the source. In the inner parts, where the ionized fraction is high ( $x_{\text{HII}} > 0.95$ ), the temperatures are of the order of  $\approx 10^5 \text{ K}$  and drops sharply in the transition zone to neutral IGM. The ionized region is restricted to about 100 kpc in physical coordinates around a halo (Thomas & Zaroubi 2008).

Figure. 2 shows  $T_s$  at four different redshifts. Collisional coupling ( $y_{\text{coll}}$ ) is important close to the radiating source ( $< 200 \text{ kpc}$ ). The primary source of coupling between  $T_s$  and  $T_k$  is the redshifting of photons blueward of the  $\text{Ly}\alpha$  line into the  $\text{Ly}\alpha$  frequency. It has to be emphasized here that the  $\text{Ly}\alpha$  photons are produced *only* due to the source and secondary processes. Thus we see that stellar sources are efficient in building up a significant background



**Figure 1.** Kinetic Temperature for stellar sources: Slices of  $T_k$  corresponding to redshifts 10, 8, 7 and 6 are plotted (panels left to right and top to bottom, respectively). Temperature are indicated in  $\log T$  [K] on the color bar above. The extent of heating, both in amplitude (maximum around  $\approx 10^5 \text{ K}$  towards the center) and spatial extent ( $< 100 \text{ kpc}$ ), is extremely small. Basically, only the central part (ionized region) is at a high temperature and falls sharply during the transition into the neutral IGM.



**Figure 2.** Spin Temperature for stellar sources: Slices correspond to that in Fig. 1. Collisional coupling is efficient to couple the  $T_k$  to  $T_s$  at the centre but the figures also indicate that there is sufficient  $J_o$  to couple  $T_k$  to  $T_s$  well beyond the ionized region, where  $T_k < T_{\text{CMB}}$ . The color bar indicates temperature on a  $\log T$  [K] scale.

of  $J_o$  far away from the source which is sufficient to couple  $T_s$  to  $T_k$  during reionization (Ciardi & Madau 2003). As an example, in Fig. 12 we show the reionization history ( $\delta T_b$ ) assuming a high background  $J_o$ , in other words, assuming perfect  $T_s - T_k$  coupling.

In Fig. 3  $\delta T_b$  corresponding to the same redshifts as in the previous figures is shown. In this particular model  $\delta T_b$  values are not very high ( $|\delta T_b| < 10 \text{ mK}$ ). At early epochs, (top-left) at  $z \approx 10$ , there are only a few sources and the heating of the IGM or the secondary  $J_o$  is not high enough to cause substantial differential brightness temperatures. At later times, the ionized bubbles over-

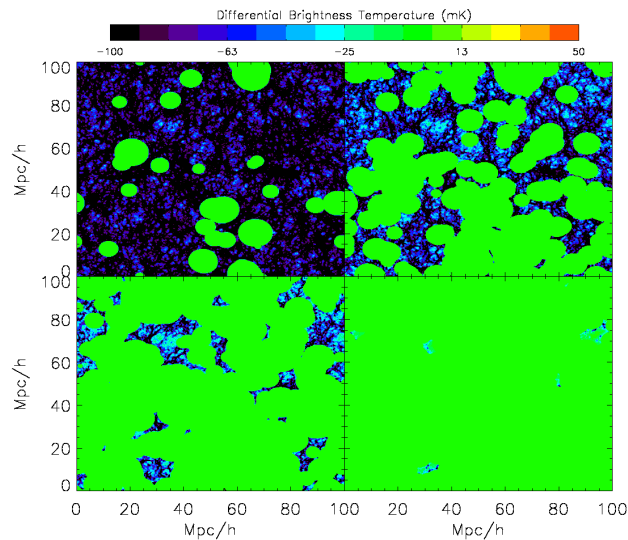


**Figure 3.** *Differential Brightness Temperature for stellar sources:* Slices corresponds to that in Fig. 1. The temperature is now contoured on a linear scale with values indicated on the colorbar. In these slices,  $\delta T_b$ , starting from zero within ionized regions attains large negative value outside because stars are not efficient at heating the IGM beyond their ionized bubble and hence cannot render the IGM visible in emission. Early on, (top-left) at a redshift of 10, there are only a few sources and the heating induced collisional coupling or the  $J_\alpha$  is not high enough to render the Universe visible, but the photons blueward of  $\text{Ly}\alpha$  can reach far outside the ionized region where they are injected into  $\text{Ly}\alpha$  frequency causing substantial coupling to the kinetic temperature which is much below the CMB. And, at later times, the ionized bubbles overlap significantly driving the brightness temperature to zero.

lap significantly driving the brightness temperature to zero. Thus there is only a small portion of the Universe (in volume) that has sufficient  $\text{Ly}\alpha$  coupling and neutral hydrogen density to cause large differential brightness temperatures. This behaviour is specific to the model assumed and will be significantly different if the parameters such as the star-formation rate, SED and escape fractions are altered.

## 4.2 Heating due to miniqsos

In this section we will consider heating due to high energy X-ray photons emanating from power-law type sources (eg., miniqsos). Because of their large mean free path ( $\propto E^3$ ) it has been difficult to incorporate the effect of heating by power-law sources self-consistently in a 3-D radiative transfer simulation.

### 4.2.1 Modeling miniqsos in BEARS

Observations reveal the energy spectrum of quasars-type sources typically follow a power-law of the form  $E^{-\alpha}$  (Vanden Berk et al. 2001; Vignali, Brandt, & Schneider 2003; Laor et al. 1997; Elvis et al. 1994). Here we assume  $\alpha = 1$  and thus the SED of the miniqsos is given by:

$$I(E) = Ag \times E^{-\alpha} \quad 10.4 \text{ eV} < E < 10^4 \text{ eV}, \quad (10)$$

with the normalization constant,

$$Ag = \frac{E_{total}}{\int_{E_{range}} I(E) dE}, \quad (11)$$

where  $E_{total}$  is the total energy output of the miniqsos within the energy range,  $E_{range}$ . Any complex, multi-slope spectral templates as in Sazonov, Ostriker, & Sunyaev (2004) can be adopted. The number of plausible SEDs that can be considered are numerous and serves as a reminder of the extent of “unexplored parameter space” even while considering the case of miniqsos alone, and argues for an extremely quick RT code like BEARS.

The miniqsos are assumed to accrete at a constant fraction  $\epsilon$  (normally 10%) of the Eddington rate. Therefore, the luminosity is given by:

$$L = \epsilon L_{\text{edd}}(M) \quad (12)$$

$$= 1.38 \times 10^{37} \left( \frac{\epsilon}{0.1} \right) \left( \frac{M}{M_\odot} \right) \text{ erg s}^{-1}. \quad (13)$$

The luminosity derived from the equation above is used to normalize the relation in Eq. 10 according to Eq. 11. The energy range considered is between 10.4 eV and 10 keV. Simulations were carried out for a range of masses between  $10^5$  and  $10^9 M_\odot$ . To justify comparing the case of stars and miniqsos we argue that, although the number of photons at different energies is a function of the total luminosity and spectral index in the case of miniqsos, if we assume that all photons from the miniqso are at the hydrogen ionization threshold, then the number of ionizing photons obtained, for the mass range fixed above, is about  $10^{50}$  to  $10^{55}$ ; the same order of magnitude as the number of ionizing photons in the case of stars and it also matches the numbers being employed for simulations by various other authors like Mellema et al. (2006) and Kuhlen & Madau (2005).

The miniqsos are embedded into an N-body output following the prescription in Thomas et al. (2009). Dark-matter haloes are identified using the friends-of-friends (FoF) algorithm and masses of black holes assigned according to,

$$M_{\text{BH}} = 10^{-4} \times \frac{\Omega_b}{\Omega_m} M_{\text{halo}}, \quad (14)$$

where the factor  $10^{-4}$  reflects the Magorrian relation (Magorrian et al. 1998) between the halo mass ( $M_{\text{halo}}$ ) and black hole mass ( $M_{\text{BH}}$ ) multiplied with the radiative efficiency assumed to be 10%, and the fraction  $\frac{\Omega_b}{\Omega_m}$  gives the baryon ratio (Ferrarese 2002).

### 4.2.2 Results: miniqsos

Contour plots of  $T_k$ ,  $T_s$  and  $\delta T_b$  for the case of *only* miniqsos being the sources of reionization, at four different redshifts, are plotted in Figs. 4, 5 and 6, respectively. The high energies of the X-ray photons substantially affects the photo-ionization and thermal energy balance of the IGM.

The marked difference between power-law type and stellar sources, in the extent to which they heat the IGM, is evident in Fig. 4. The temperatures are shown at redshifts 10, 8, 7 and 6 with ionized fractions 0.01, 0.54, 0.96, 0.999 respectively. In the inner parts of the “ $T_k$  bubble” the amplitude of  $T_k$  is about  $\approx 10^{6.5}$  K. The secondary electrons created by high energy X-ray radiation thermalizes to these high temperature values. Also contributing to extremely high temperatures in the very inner parts of the bubble is Compton heating (Thomas et al. 2009). The mean free path of X-rays are extremely large resulting in a spatial extent of heating that reaches many Mpcs. Thus, we see that already at redshift 10 (top-left) the average temperature of the IGM is of the order of  $10^3$  K and overlap of the temperature bubbles occur much before that of the ionization bubble. This example might be unrealistic, because

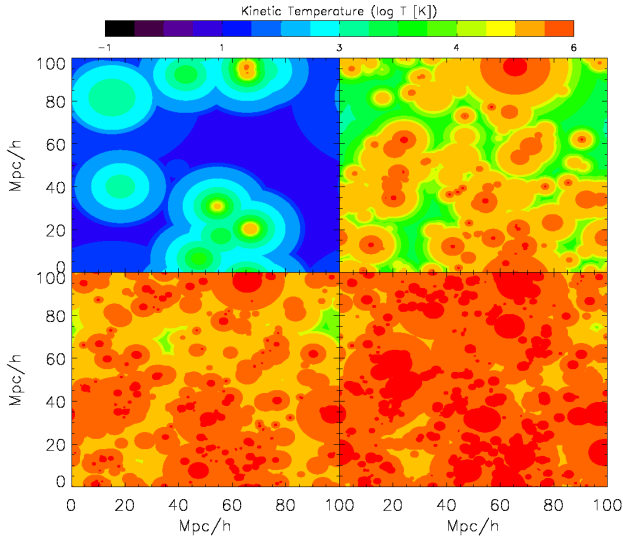


**Figure 4.** Kinetic Temperature for miniqso sources: Slices correspond to that in Fig. 1 with temperatures indicated on a log T [K] scale. Here we see the striking difference between miniqsos and stars in the extent of heating. The amplitude is about  $\approx 10^{6.5}$  K towards the center and spatial extent of the heating is about a few Mpc. Already at redshift 10 (top-left) the average temperature is of the order  $10^3$  K.

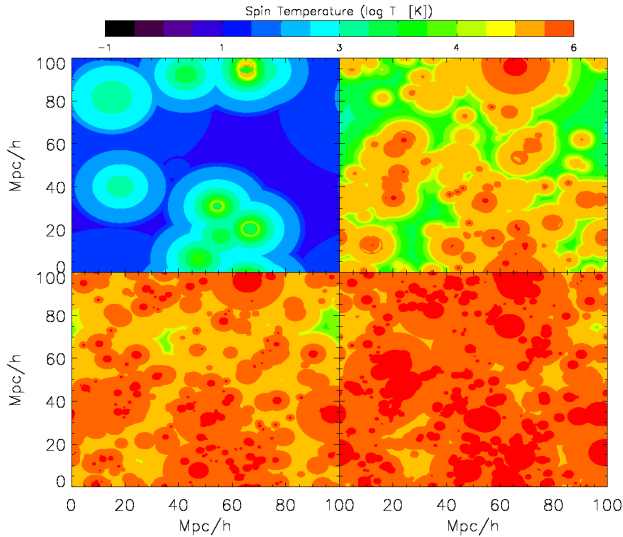


**Figure 5.** Spin Temperature for miniqso sources: Slices correspond to that in Fig. 1 with the temperatures indicated on a log T [K] scale. Spin temperatures show an interesting ring-like behaviour (easily visible in the top-left panel). The reason for this is discussed in the text.

the soft X-ray background constraint (Dijkstra, Haiman, & Loeb 2004) is not strictly observed, but again this serves just as an illustrative example.

Figure. 5 shows the evolution of  $T_s$  as a function of redshift. Owing to a high secondary  $J_o$  produced due to X-ray photons,  $T_s$  is coupled to  $T_k$  for the large part. The snapshots of  $T_s$  show a peculiar ring-like behaviour (Refer. Fig. 5). This is because towards the central part of the bubble around the source, the IGM is highly ionized and  $J_o \propto x_{\text{HII}}$ , obtains an extremely low value. On the other hand  $J_o$  progressively gets lower away from the source, regions ( $>5$ Mpc). Therefore only a relatively narrow zone (few hundred

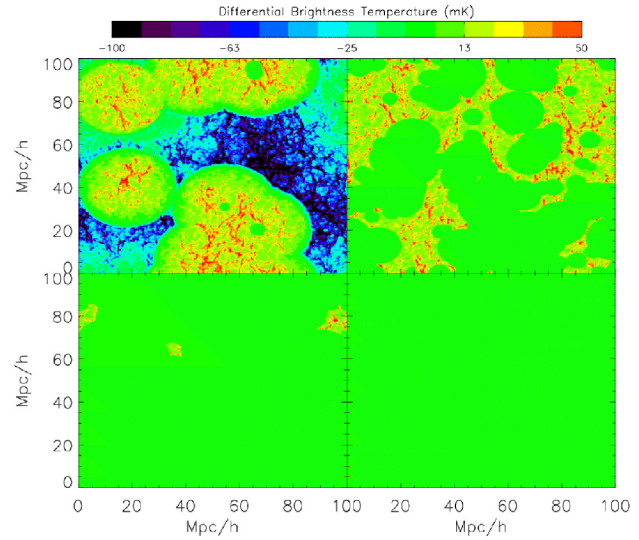


**Figure 6.** Differential Brightness Temperature for miniqso sources: Slices correspond to that in Fig. 1. Note here that the brightness temperature (mK) in plotted on a linear scale with values as indicated on the color bar. We see again from the top-left panel that although the number of sources in the field are few, they were efficient in both increasing  $T_k$  dramatically and providing sufficient  $J_o$  to “light-up” the Universe in 21-cm around them. The spheres in the top-left panel have  $\delta T_b$  of zero because they are highly ionized.

kpc) in between the ionizing front and regions further out has  $J_o$  high enough to decouple  $T_s$  from  $T_{\text{CMB}}$ .

Figure. 6 shows  $\delta T_b$  for redshifts 10, 9, 8 and 7 in panels top-left to bottom-right, respectively. The  $\delta T_b$  plotted in this figure are high enough to be detectable by upcoming telescope’s like LOFAR and MWA, whose sensitivities should reach  $\delta T_b > 5$ mK (Labropoulos et al. 2009). We see in the top-left panel of this figure that even though the number of sources in the field is small, they are efficient in both increasing  $T_k$  dramatically and providing sufficient  $J_o$  to “light-up” the Universe in the 21-cm differential brightness temperature. The  $\delta T_b$  inside the spheres are zero because they are highly ionized ( $x_{\text{HII}} > 0.99$ ).

### 4.3 Modeling co-evolution of stars & miniqsos

In the observable Universe we know that stars and quasars do co-exist. Although, there are indications of the quasar number-density peaking around redshift two (Nusser & Silk 1993) and declining thereof, there are also measurements by Fan et al. (2006) of high-mass ( $> 10^8 M_\odot$ ) quasars at  $z > 6$ . This allows us to envisage a scenario of reionization in which stars and quasars (or miniqsos) contributed to the ionization and heating of the IGM in a combined fashion. As a final example-application of BEARS, we present our model of a “hybrid” star-miniqso SED and examine its results on the ionization and heating of the IGM.

#### 4.3.1 The “Hybrid” SED

The uncertainty regarding the properties and distributions of objects during the dark ages allows us to come up with strikingly different ways of incorporating the co-existence of stars and miniqsos. For example, consider that there are  $\mathcal{N}$  different haloes within our simulation box. One approach would be to suppose that each of these haloes host both a miniqso and stars, whose

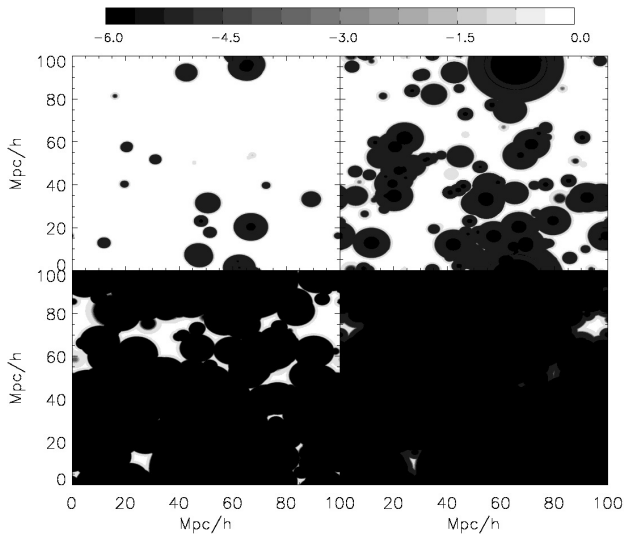


**Figure 7.** *Ionization due to the hybrid model:* Slices correspond to that in Fig. 1. Shown in these slices are the contour levels of neutral hydrogen in a logarithmic scale. We see here that for the hybrid model we have assumed the ionization proceeds quickly and the Universe is substantially ionized by redshift 6 (Refer Fig. 11) for the reionization history. The extent of ionizations interpolates between the cases of black holes and stars.

masses/luminosity is derived according to the previous two examples. The other approach would be to place one or two massive miniquas (almost quasars), still conforming to the black hole mass density predictions of Volonteri, Lodato, & Natarajan (2008), and the rest of the haloes in the simulation box with populations of stars. For this example, given the minimum mass halo our simulation can resolve, we have chosen to adopt the former approach, i.e., a miniquiso and stars in every halo.

In our approach, given the halo mass we embed them with stellar sources as described in §4.1.1. Then the black hole mass is set as  $10^{-4}$  times the stellar mass. Radiative transfer is performed using this hybrid SED, i.e., a superposition of power-law type miniquiso SED and black body spectrum normalized according to the criterion in the previous sections. The results of ionization and heating are presented below.

#### 4.3.2 Results: Hybrid model

The hybrid model proposed does have large amounts of high-energy X-ray photons from miniquasos that influence the temperature and ionization of the IGM prior to full reionization. The X-rays photons have larger mean free paths than their UV counterparts, and their secondary electrons have significant influence on the thermal and ionization balance. The UV photons on the other hand are efficient at keeping the IGM in the vicinity of the halo highly ionized. For the redshifts 10, 8, 7 and 6 we plot the ionization due to the hybrid model in Fig. 7 and the ionized fraction at these redshifts are 0.01, 0.38, 0.86 and 0.995 respectively.

For this hybrid model the number of UV photons was not high enough to ionize the Universe completely by redshift 6 (the ionized fraction reaches 0.95). Full reionization thus could be achieved either by increasing the mass of the black hole and/or by changing the ratio between the black hole and stellar masses.

The hybrid model considered here yielded  $T_k$ ,  $T_s$  and  $\delta T_b$  as in Figs. 8, Fig. 9 and Fig. 10, respectively.

The hybrid model produces heating patterns that interpolates

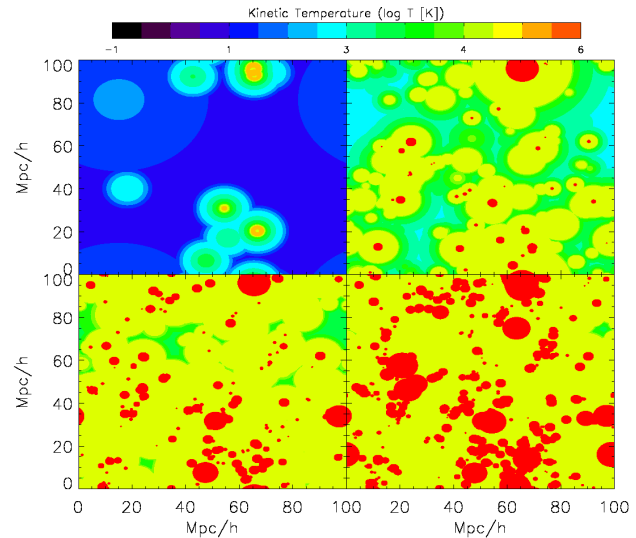


**Figure 8.** *Kinetic temperature for hybrid model:* Slices correspond to that in Fig. 1, with temperatures indicated on a log  $T$  [K] scale. The heating pattern is peculiar in that the temperature shows a much “cuspy” behaviour towards the center. The reason is that the stellar component of the source ionized the very central part and the X-ray radiation can thus heat the central part where to even higher temperature. On the other hand the large extent of the heating is attributed to the power-law component of the SED.

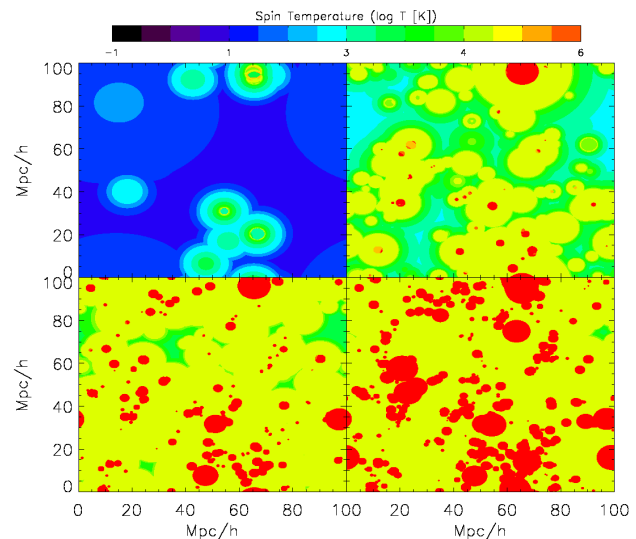


**Figure 9.** *Spin temperature for the hybrid model:* Slices correspond to that in Fig. 1. Spin temperatures for the case of the hybrid model again shows the ring like behaviour as in the case of power-law sources. Temperatures are indicated on a log  $T$  [K] scale.

between the results for the previous two cases and thus is qualitatively different (Fig. 8). The power-law components take over the role of heating an extended region and the stellar component maintains a very high temperature in the central parts.

The spin temperature (Fig. 9) again shows the characteristic ring-like structure around the source. The amount of secondary Ly $\alpha$  radiation produced due to the miniquasos results in an efficient coupling of the spin temperature and the kinetic temperature.

The brightness temperature for the hybrid model is plotted in Fig. 10. The secondary  $J_\alpha$  produced due to the power-law component efficiently couples the high ambient  $T_k$  of the IGM to  $T_s$

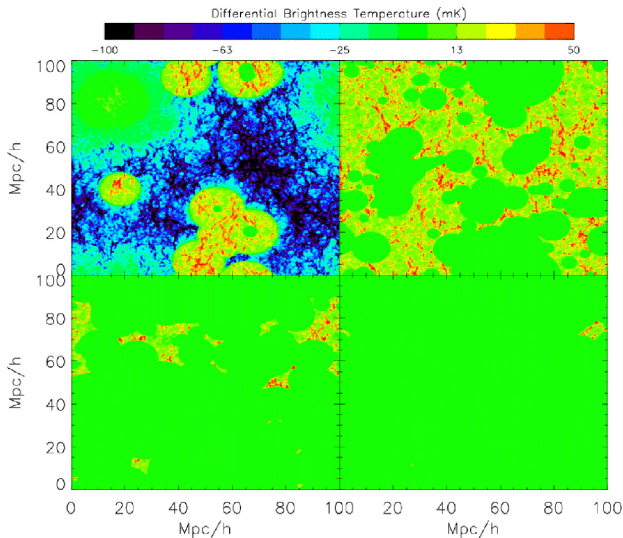


**Figure 10.** *Differential Brightness temperature for the hybrid model:* Slices correspond to that in Fig. 1. The temperatures (mK) are indicated on a linear scale in the color bar above. The large extent of heating and sufficient  $J_{\alpha}$  ensures that the IGM well beyond the location of the source is rendered visible in 21-cm emission.

and this enables a large fraction of the Universe to be visible in the brightness temperature albeit with a few sources (top-left panel of the figure). The brightness temperature does not go to zero at redshift six because, in the model we have assumed, the Universe is not entirely ionized by then (for recent papers on this issue see Mesinger (2009)).

#### 4.4 Reionization histories: A comparison

In this section we compare the reionization histories for the three scenarios explored above. To create a contiguous observational cube or “frequency cube” (right ascension (RA)  $\times$  declination (DEC)  $\times$  redshift), we adopt the procedure described in Thomas et al. (2009). The procedure involves the stacking of RA and DEC slices, taken from individual snapshots at different redshifts (or frequency), interpolated smoothly to create a reionization history. This data cube is then convolved with the point spread function of the LOFAR telescope to simulate the mock data cube of the redshifted 21-cm signal as seen by LOFAR. For further details on creating this cube refer to Thomas et al. (2009).

As expected the signatures (both visually and in the r.m.s) of the three scenarios (Fig. 11) are markedly different. In the miniqso-only scenario, reionization proceeds extremely quickly and the Universe is almost completely ( $\langle x_{\text{HII}} \rangle \approx 0.95$ ) reionized by around redshift 7. The case in which stars are the only source see reionization end at a redshift of 6. Also in this case, compared to the previous one, reionization proceeds in a rather gradual manner. The hybrid model, as explained previously, interpolates between the previous two scenarios.

The  $\delta T_{\text{b}}$  in Fig. 11 is calculated based on the effectiveness of  $J_{\alpha}$ , produced by the source, to decouple the CMB temperature ( $T_{\text{CMB}}$ ) from the spin temperature ( $T_{\text{s}}$ ). This flux, both in spatial extent and amplitude, is obviously much larger in the case of miniqsos compared to that of stars resulting in a markedly higher brightness temperatures in both the miniqso-only and hybrid models when compared to that of the stars. However, we know that stars themselves produce  $\text{Ly}\alpha$  radiation in their spectrum. Apart

from providing sufficient  $\text{Ly}\alpha$  flux to their immediate surrounding, this radiation builds up, as the Universe evolves, into a strong background  $J_{\alpha}$  (Ciardi & Madau 2003), potentially filling the Universe with sufficient  $\text{Ly}\alpha$  photons to couple the spin temperature to the kinetic temperature everywhere. Thus, we plot in Fig. 12 the same set of reionization histories as in Fig. 11 but now assuming that  $T_{\text{s}}$  coupled to  $T_{\text{k}}$ . Clearly the “cold” regions in the Universe show up as regions with large negative brightness temperature. This assumption though is not strictly applicable towards the beginning of reionization. In §5 we quantify the differences in the brightness temperature evolution when this assumption is made.

It has to be noted that the results we are discussing here are extremely model dependent and any changes to the parameters can influence the results significantly. This on the other is the demonstration of the capability and the need for a “BEARS like” algorithm to span the enormous parameter space of the astrophysical unknowns in reionization studies.

#### 4.5 Looking through LOFAR

To test the feasibility of 21-cm telescopes (specifically LOFAR) in distinguishing observational signatures of different sources of reionization, we need to propagate the cosmological 21-cm maps generated in §4.4 using LOFAR’s telescope response. The point spread function (PSF) of the LOFAR array was constructed according to the latest configuration of the antenna layouts for the LOFAR-EoR experiment.

The LOFAR telescope will consist of up to 48 stations in The Netherlands<sup>8</sup> of which approximately 22 will be located in the core region (Labropoulos et al. 2009). The core marks an area of  $1.7 \times 2.3$  kilometres and is essentially the most important part of the telescope for an EoR experiment. The core station consists of two sets of antennae, the Low Band (LBA; 30-90 MHz) and the High Band Antenna (HBA; 110-240 MHz). The HBA antennae in the core stations is further split into two “half-stations” of half the collecting area (35-metre diameter), separated by  $\approx 130$  metres. This split further improves the uv-coverage. For details on the antenna layout and the synthesis of the antenna beam pattern refer to upcoming paper by Labropoulos et al. (2009).

In its current configuration, the resolution of the LOFAR-core is expected to be around 3 arcmins. Thus, as an example at redshift 10, all scales below  $\approx 800$  kpc will be filtered out. Fig. 13 shows this effect for the reionization histories corresponding to Fig. 11. The corresponding changes in the r.m.s of the brightness temperature is also plotted. We see that, although smoothed to a large extent, there still exists qualitative differences between the different scenarios. This of course is a reflection of the vastly contrasting models of reionization compared in this paper and difference will disappear if the models investigated are more similar to each other.

## 5 STATISTICAL ANALYSIS OF THE SIMULATIONS

The previous section provided a qualitative description of the differences in the 21-cm  $\delta T_{\text{b}}$  fluctuations for two cases i.e., with and without the assumption that  $T_{\text{s}} = T_{\text{k}}$ . In this section, a number of statistical tests are performed to quantify these differences. For this

<sup>8</sup> This is decision under review and might change subsequently.

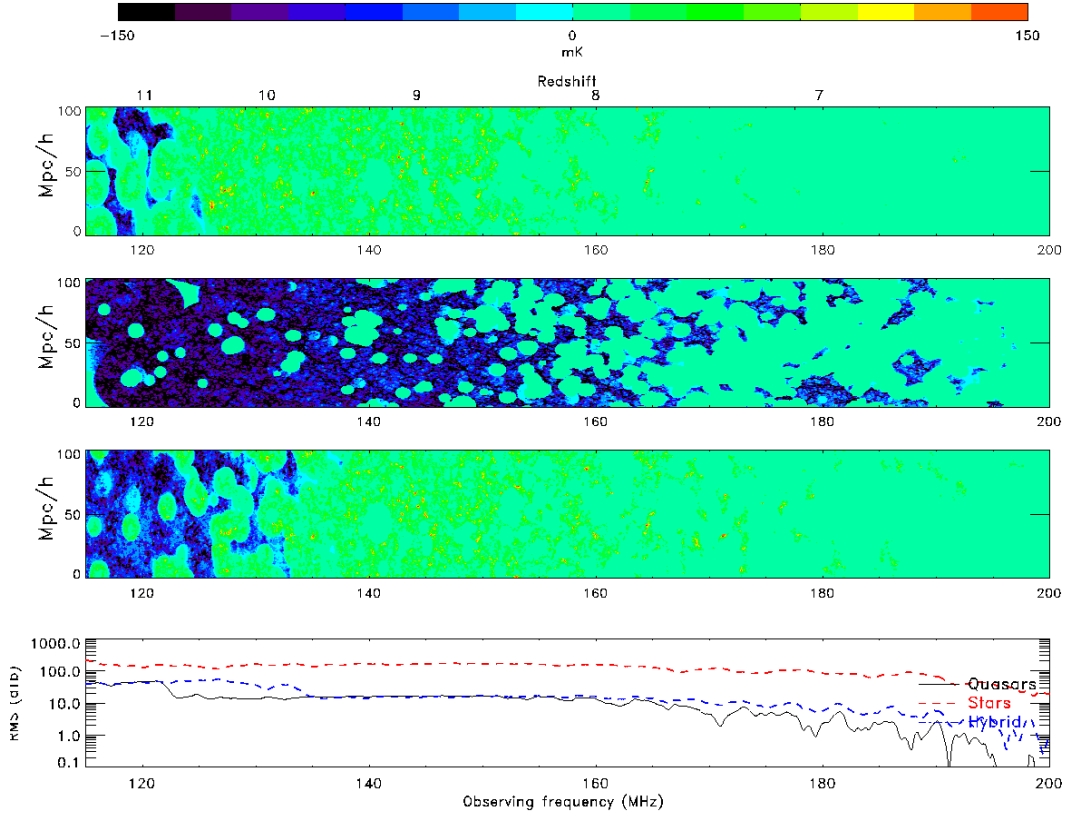


**Figure 11.** *Contrasting reionization histories:* From the top, reionization histories ( $\delta T_b$  in mK as a function of frequency or redshift) are plotted for miniqso, stellar and hybrid sources, respectively. The bottom panel plots the r.m.s. of  $\delta T_b$  as a function of redshift/frequency for all the three cases.

purpose we focus on the scenario with the miniqsos. This exercise can be repeated for the other two scenarios as well.

Firstly, Fig. 14 shows the 3-D power spectra of  $\delta T_b$  at redshift 12, 10, 8 and 6. In our model, reionization begins at around redshift 12.7 and thus  $z=12$  can be considered the onset of reionization. The dashed curve reflects the assumption that  $T_s = T_k$  while the solid curve takes into account the evolution of  $T_s$  self-consistently. At the initial stages of reionization, only regions at close proximity to the source have been ionized and heated, and the volume filling by “spheres of ionization” has just begun, leaving large portions of the Universe neutral and cooler than the CMB. Here we assume that after the epoch of recombination the Universe cools adiabatically, i.e.,  $T_k \propto 1/(1+z)^2$  and  $T_{\text{CMB}} \propto 1/(1+z)$ , which results in  $T_k \ll T_{\text{CMB}}$  at the onset of reionization. Thus, we have a situation in which we have assumed  $T_s = T_k$ , with  $T_k \ll T_{\text{CMB}}$ , resulting in an *artificial* decoupling of  $T_s$  and  $T_{\text{CMB}}$ , and is manifested as increased 21-cm power. The discrepancy quickly (by  $z = 10$ ) disappears as the “spheres of Ly $\alpha$ ” overlap to volume-fill the simulation box and hence increase the  $T_s - T_k$  coupling efficiency. Therefore, in our model, it is safe to make the assumption that  $T_s$  follows  $T_k$  after about  $z = 10$ .

From Eq. 6 it follows that  $\delta T_b$  attains large negative values when two conditions are satisfied,  $T_s \ll T_{\text{CMB}}$  and a high neutral hydrogen overdensity. We therefore plot the mean, minimum and maximum values of  $\delta T_b$  as a function of redshift in Fig. 15. As expected the mean and minimum values of  $\delta T_b$  are much lower for the case in which the spin temperature has been set to the kinetic temperature, because the Universe has cooled substantially

below the CMB and coupling  $T_k$  everywhere in the Universe to  $T_s$  enforces the conditions required for large negative  $\delta T_b$  as stated above. The maximum positive values though do not differ because a positive  $\delta T_b$  indicates that  $T_s > T_{\text{CMB}}$  and hence has to be heated by the radiating source. And in regions where the source has heated the IGM, the presence of Ly $\alpha$  flux and collisional coupling almost always guarantees the coupling of  $T_s$  to  $T_k$  anyway.

As another simple diagnostic of the efficiency of  $T_s - T_k$  coupling we plot, (i) the differential temperature, i.e.,  $1 - T_{\text{CMB}}/T_s$ , (ii) their ratio,  $T_k/T_s$ , as a function of redshift (Fig. 16). Note here that if the spin temperature was artificially set to the kinetic temperature, the differential temperature would be saturated at unity. But the coupling ensures that the spin temperature remains below that of the CMB till about a redshift of 10. Although significantly different at the early phases of reionization, in the model we have assumed,  $T_s$  catches up with  $T_k$  at a redshift of about eight, when the coupling due to Ly $\alpha$  and collisions become significant enough to tie  $T_s$  to the local  $T_k$ .

As an alternative probe to investigate the influence of Ly $\alpha$ -coupling coupling, in Fig.17 we plot the power spectra, now of the kinetic (solid line) and the spin (dashed line) temperatures at four different redshifts. There are a few interesting attributes to this figure. Firstly we see that at all scales  $T_s$  is considerably lower than  $T_k$  at the onset of reionization ( $z \approx 12$ ). This scenario changes rapidly as  $T_s$  approaches  $T_k$ . Note that it is only towards the end of reionization ( $z=6$ ) that  $T_s$  is identical to  $T_k$  at all scales. The peculiarity observed is that all scales in  $T_s$  do not approach  $T_k$  simultaneously. As seen from the top two panels of the figure at

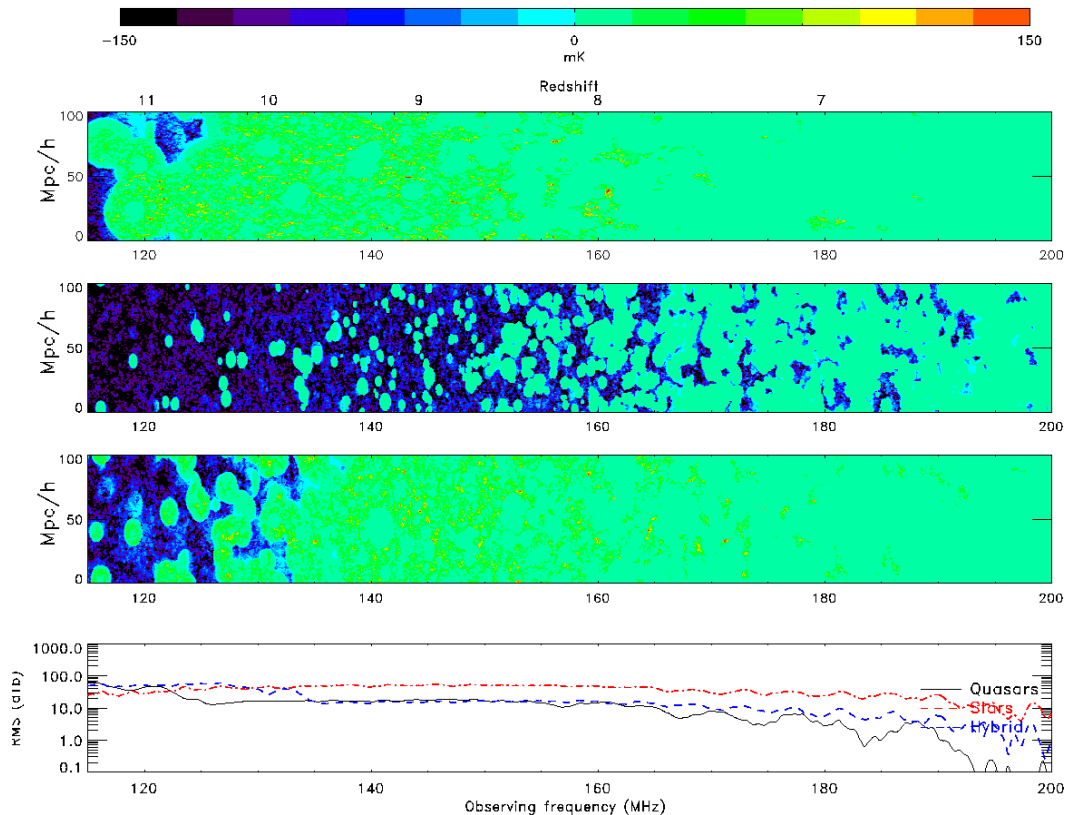


**Figure 12.** Reionization histories assuming  $T_s = T_k$ : Reionization histories ( $\delta T_b$ ), same as in Fig. 11 are plotted, now with the assumption that the  $T_s$  has been completely decoupled from  $T_{\text{CMB}}$ .

$z = 10$  and  $z = 8$ ,  $T_s$  approaches  $T_k$  at large scales (small  $k$  values). And then subsequently at small scales towards the end of reionization. This is because the central parts of the ionized bubble around the source was highly ionized and because  $J_o \propto x_{\text{HI}}$ , the spin temperature obtains extremely low values. Now, as you go further away from the source, the IGM becomes neutral, but  $J_o$  from the source and the secondary  $\text{Ly}\alpha$  photons is high enough to couple the spin temperature to the kinetic temperature. Thus, the large scales (large volumes outside the ionized bubble) get “matched” first followed by the small scales, when the IGM is hot and collisions become important.

### 5.1 Comparison to similar work

Here we briefly compare the output of our simulation with that of Santos et al. (2008), wherein a semi-analytical scheme is developed to look at ionization and heating during the epoch of reionization. Fig.18 shows the comparison between our simulations which has now been performed for the case of a power-law source starting at 100eV to facilitate a balanced comparison with the 100eV case of Santos et al. (2008). Plotted in this figure are the average gas temperature (solid line and crosses) and volume filling factor of X-ray radiation (dashed line and filled hexagons). The lines correspond to our simulation and points to Santos et al. (2008). Their case with the normalization factor  $f_x = 10$ ,<sup>9</sup> and photon energies of 100.0

<sup>9</sup> Santos et al. (2008) normalized their spectrum assuming a total integrated power density to be  $3.4 \times 10^{40} f_x \text{ ergs/s/Mpc}^3$ .

eV shows similar trends. Because we start reionization a bit later ( $z = 12$ ) the temperature is a bit lower initially. Their model is qualitatively different because the X-ray emissivity is tied to their star-formation rate. Otherwise, the manner in which heating is implemented to similar to the one described in our case albeit without terms involving compton heating/cooling. These effects though are important towards the central regions of the source (Thomas & Zaroubi 2008).

## 6 CONCLUSIONS & OUTLOOK

The focus of this paper was three-fold. 1) to introduce an extension to BEARS in order to incorporate heating (including X-ray heating) and discuss its application to two cases of reionization and heating, i.e., for blackbody (stellar) and power-law (miniqso) type sources, 2) to monitor the evolution of spin temperature ( $T_s$ ) self-consistently and contrast its influence against the usual assumption made in most reionization simulation that  $T_s \gg T_{\text{CMB}}$ , and 3) use the extended BEARS code to study reionization due to a hybrid population of stars and miniqsos as reionizing sources.

To incorporate heating into BEARS, we embedded spheres of “kinetic temperature” around the sources of radiation, much like in the algorithm used to obtain the ionized fraction (Thomas et al. 2009). The BEARS algorithm implemented is extremely fast, in that it takes  $\sim 5$  hours (2GHz, 16-core, 32GB shared RAM) to perform the radiative transfer (including heating) on about 35 different boxes ( $512^3$  and  $100 h^{-1}$  comoving Mpc) between redshifts 12 and 6. These snapshots are interpolated between redshifts to pro-

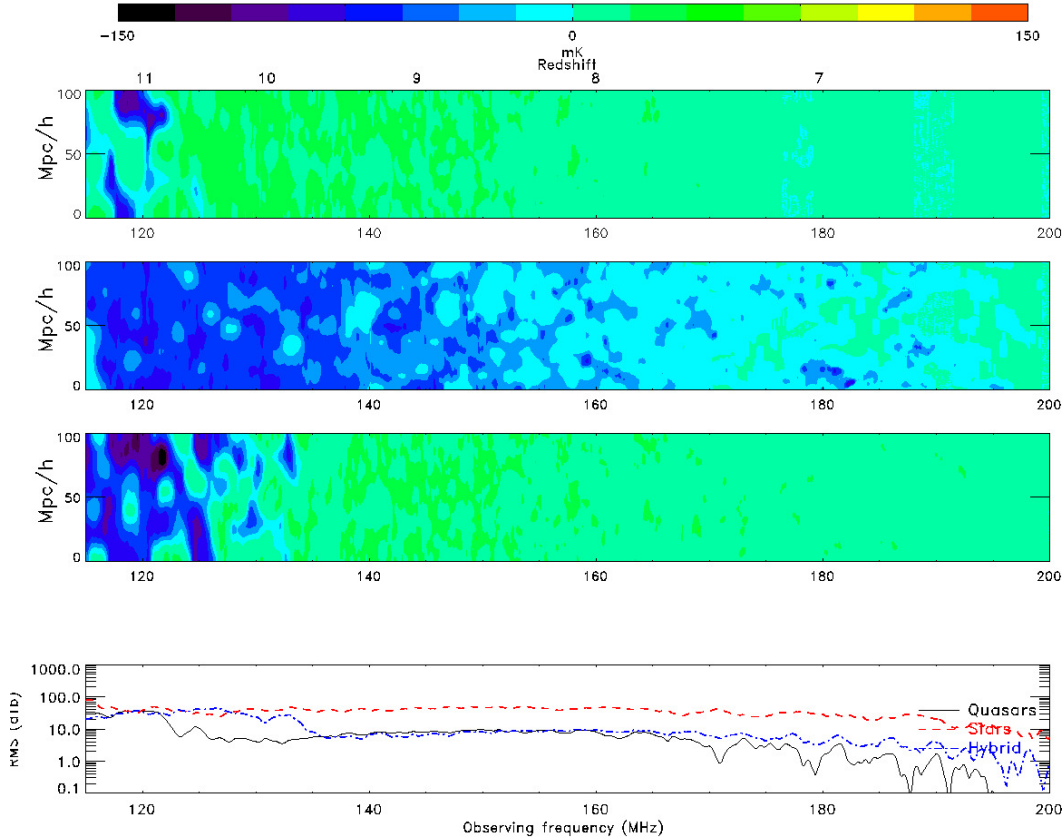


**Figure 13.** Convolution with LOFAR - PSF: Differential brightness temperatures after convolution with a point spread function corresponding to LOFAR is plotted for the same case as in Fig. 11, with the temperatures plotted in mK.

duce a contiguous data cube spanning redshifts  $z \approx 6 - 12$ , i.e., the observational range of the LOFAR-EoR experiment. The efficiency of the code facilitates the simulation of many different scenarios of reionization and test their observational signatures. Apart from predicting the nature of the underlying cosmological signal, these simulations can be used in conjunction with others probes of reionization to enhance the detectability and/or constrain parameters concerning reionization. In Jelic et al. (2009) these simulations were cross-correlated with the simulations of the CMB anisotropy (mainly the kinetic and thermal SZ-effect) to probe reionization. In the same paper Jelic et al., repeated the same exercise by using reionization simulations from Mellema et al. (2006) and found similar results, further emphasizing the validity of the approximate manner in which we solve the evolution of the kinetic temperature in our simulations.

The improved BEARS code was used to simulate three distinct reionization scenarios, i.e., miniqsos, stellar and a mixture of both. These simulations further emphasized that miniqsos were not only very efficient in increasing  $T_k$  of the IGM but the secondary Ly $\alpha$  flux produced by these sources was enough to drive  $T_s$  away from  $T_{CMB}$  in an extended region around the source thereby rendering the IGM around the source “bright” in  $\delta T_b$ . This implies, if a miniqso hosting a black hole in the mass range  $> 10^7 M_\odot$  is within the observing window of LOFAR, the value of  $\delta T_b$  and its spatial extent would be conducive to a possible detection. The code was also applied to simulate reionization with a hybrid population of stars and miniqsos. Every dark matter halo was embedded with both a quasar and a stellar component. The relation between the two

was set according to the “Magorrian relation” we observe today. The total mass in quasars were constrained following black hole mass density estimates by Volonteri, Lodato, & Natarajan (2008). The effect of the hybrid population on the IGM was an interpolation between the scenarios of stars and miniqsos i.e., although the heating (and ionization) was not as extended as in the case of miniqsos, it was definitely larger than that for stars.

Our ultimate goal is to simulate mock data sets for the LOFAR-EoR experiment. Towards this end, reionization simulations performed on 35 different snapshots between redshifts 6 and 12 were combined to form “frequency cubes” (reionization histories, Thomas et al. (2009)) for all three scenarios i.e., stars, miniqsos and the hybrid case. To fold-in the effect of the instrument we smoothed these frequency cubes according to the LOFAR beam-scale. Notwithstanding the convolution by the LOFAR beam, stark differences between the scenarios clearly persists. The r.m.s  $\delta T_b$  clearly shows this difference between scenarios.

All three scenarios of reionization discussed above was performed for two different cases, i) assuming that  $T_s$  is always coupled to  $T_k$  and ii) following the evolution of  $T_s$  self-consistently in the simulation. Figures 11 and 12 reflect the differences between the two cases. To further quantify the influence of the self-consistent evolution of  $T_s$ , especially at the beginning of reionization, a suite of statistical analyses was performed<sup>10</sup>. Firstly, the 3-D power spectra of  $\delta T_b$  (Fig. 14) for the two cases was calcu-

<sup>10</sup> Although these tests are specific to the scenario with miniqsos, it can be repeated for the case of stars and the hybrid. Miniqsos were chosen since

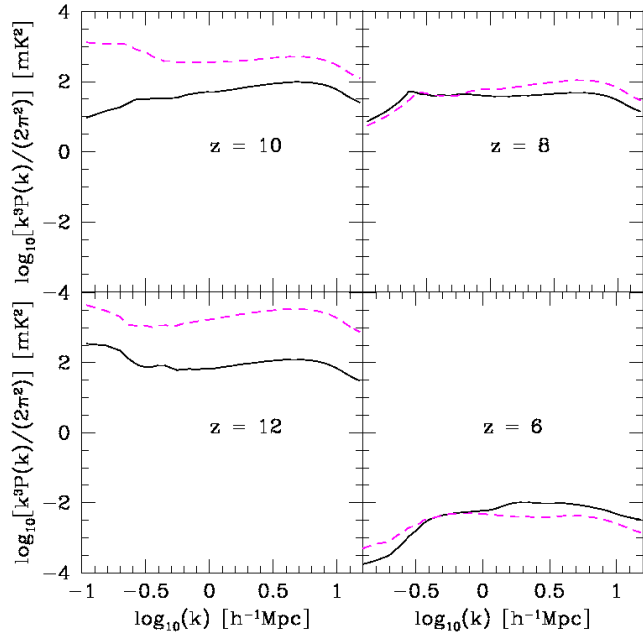


**Figure 14.** The 3-D power spectra of  $\delta T_b$  at four different redshifts (as indicated on the panels) are plotted. The solid curves indicate the power spectra resulting from the self-consistent inclusion of  $T_s$  and the dashed curve, under the assumption  $T_s = T_k$ . At the onset of reionization,  $z \approx 12$  in our model,  $\delta T_b$  is larger at all scales under this assumption because we have enforced, in effect, an *artificial* decoupling of  $T_s$  from  $T_{\text{CMB}}$  in regions of the simulated Universe where  $T_k \ll T_{\text{CMB}}$ . But by redshift 10 the power spectra match exactly as the  $\text{Ly}\alpha$  becomes efficient everywhere in the box to couple  $T_s$  to  $T_k$ . Notice that the power keeps dropping as  $x_{\text{HI}} \rightarrow 0$  and Universe gets reionized at lower redshifts.

lated at four redshifts (12, 10, 8 and 6). We see that although there is a considerable difference at the onset ( $z=12$ ) of reionization the power spectra of the brightness temperature match-up by a redshift of 8. This is attributed to the volume filling nature of the spin temperature coupling induced by miniqsos. The minimum, maximum and mean value of  $\delta T_b$  as a function of redshift reveal similar differences between the two cases. The maximum value of  $\delta T_b$  is the same in both cases because regions where the IGM is considerably heated also corresponds to regions with a large supply of  $\text{Ly}\alpha$  photons and they are also regions where collisional coupling is effective. The minimum and average values reveal a difference since under the assumption that  $T_s = T_k$ , regions much below  $T_{\text{CMB}}$  are artificially coupled to  $T_s$ . As a final statistic we compute the 3-D power spectra of  $T_k$  and  $T_s$  and compare them (Fig. 17). Vast differences do exist between the two almost till the end of reionization, when they become identical. An interesting result of this comparison is that the large scales of the two spectra get matched before the small scales in the box. The interpretation of this behaviour is given in section 5. We also compared our results to that of Santos et al. (2008) and found good match for the evolution of gas temperature and the volume filling factor of X-ray radiation.

In the near future calibration errors expected from a LOFAR-EoR observational run will be added to these simulations along with the effects of the ionosphere and expected radio frequency

in this case we observe the largest difference due to of the copous amounts of secondary  $\text{Ly}\alpha$  flux and heating induced by miniqsos.

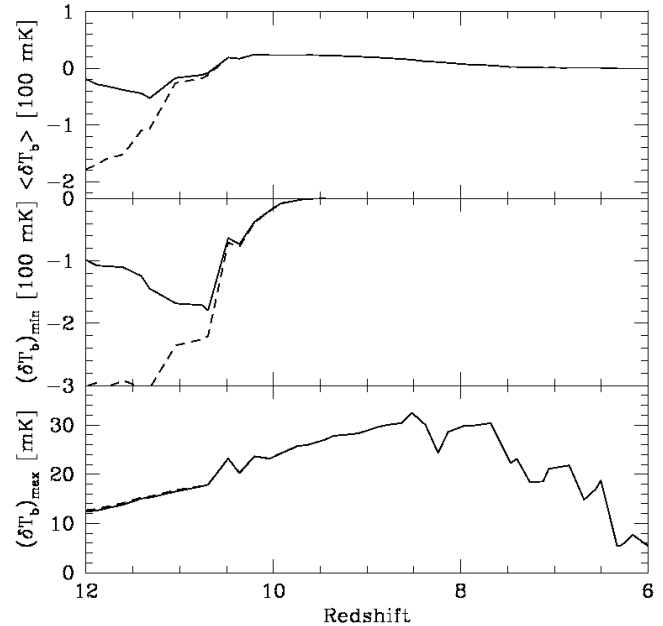


**Figure 15.** Plotted above are the mean (top), minimum (middle) and maximum (bottom) values of  $\delta T_b$  as a function of redshift. Line styles correspond to Fig.14. Because at earlier redshifts (around 12)  $T_k \ll T_{\text{CMB}}$  within a large fraction in the simulation box, the minimum value attained by assuming  $T_s = T_k$  is much lower than when only regions with  $\text{Ly}\alpha$  excitation (which is typically near the source) is allowed to couple  $T_s$  with  $T_k$ . And for the same reason the maximum value in both cases are similar because the assumption holds close to the sources as the presence of  $\text{Ly}\alpha$  flux ensures efficient coupling. As a result the global average  $\delta T_b$  is also lower for the approximated model at the onset of reionization and catches up quickly to the “proper” model as the Universe fills up with sufficient  $\text{Ly}\alpha$  flux.

interference (RFI). Subsequently, Galactic and extra-galactic foregrounds modeled as in Jelić et al. (2008) will be merged with these simulations to create the final “realistic” data cube. These data cubes will be processed using the LOFAR signal extraction and calibration schemes being developed to retrieve the underlying cosmological signal in preparation for the actual LOFAR-EoR experiment which has already begun.

## 7 ACKNOWLEDGMENT

The author RMT would also like to thank the Institute for the Physics and Mathematics of the Universe, Tokyo, for the support provided during an extended stay. LOFAR is being partially funded by the European Union, European Regional Development Fund, and by “Samenwerkingsverband Noord-Nederland”, EZ/KOMPAS. The authors would like to thank the anonymous referee was his/her extensive comments on the manuscript and for improving its contents significantly. RMT and SZ would also like to thank Joop Schaye and Andreas H. Pawlik for providing us with the N-body simulations and for useful discussions.

## REFERENCES

- Abel T., Bryan G. L., Norman M. L., 2002, *Science*, 295, 93  
 Abel T., Bryan G. L., Norman M. L., 2000, *ApJ*, 540, 39

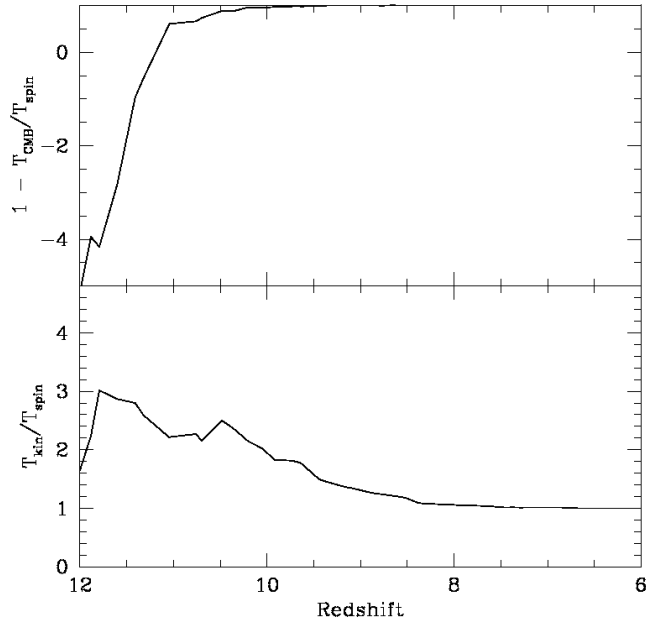


**Figure 16.** The differential temperature  $(T_{\text{spin}} - T_{\text{CMB}})/T_{\text{spin}}$  (top) and the ratio,  $T_{\text{kin}}/T_{\text{spin}}$  (bottom), are plotted as a function of redshift. If  $T_{\text{spin}}$  was assumed to track  $T_{\text{kin}}$ , then the top panel would always be saturated at unity. The kinetic temperature likewise merge with the spin temperature only by a redshift of  $z = 8$ , as seen in the bottom panel.

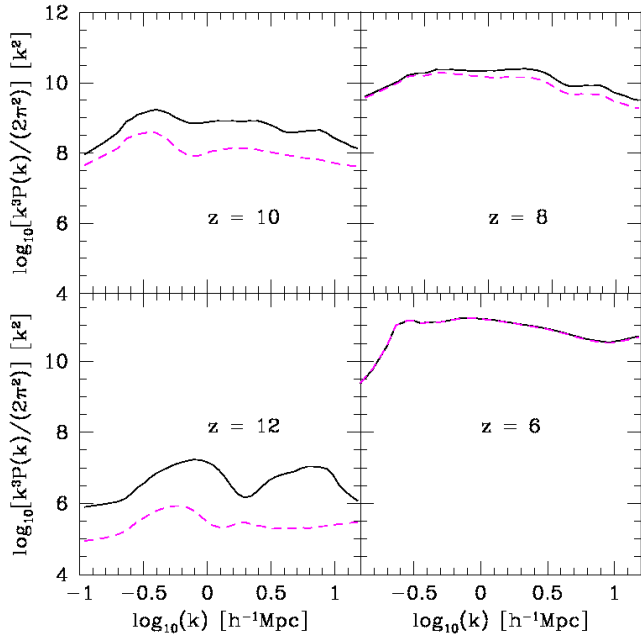


**Figure 17.** At four different redshifts are plotted the power spectra of the kinetic temperature (solid) and the spin temperature (dashed) within the simulation box. Note how the  $T_s$  is considerably lower than the  $T_k$  initially and then merges with  $T_k$  as reionization proceeds. Refer text for more details.

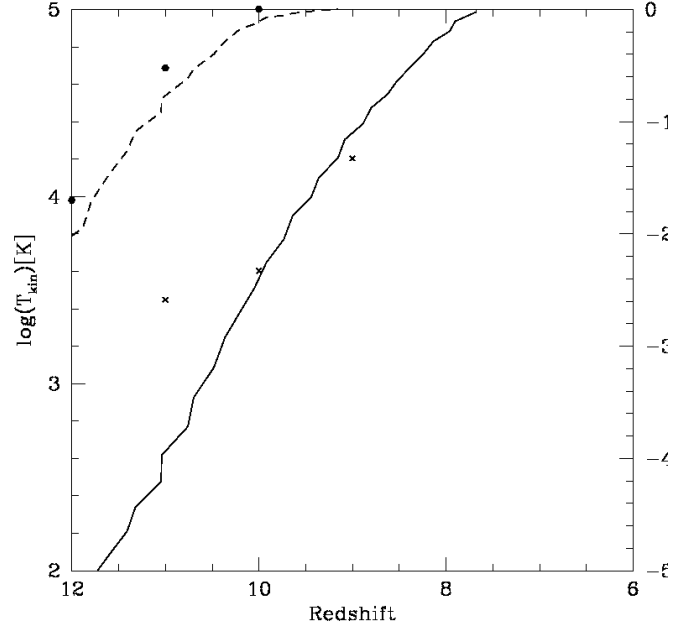


**Figure 18.** Plotted here are the evolution of the gas temperature  $T_k$  (solid line) and the volume filling factor (dashed line) of the X-ray radiation as a function of redshift for the case of the miniquas. For comparison, points from Santos et al. (2008) are shown for  $T_k$  (crosses) and filling factor (filled hexagons) with their case of  $f_x = 10$  and photon energies 100.0 eV.

- Baek S., Di Matteo P., Semelin B., Combes F., Revaz Y., 2009, *A&A*, 495, 389  
 Bromm, V., Coppi, P.S., Larson, R.B., 2002, *ApJ*, 564, 23  
 Chuzhoy L., Alvarez M. A., Shapiro P. R., 2006, *ApJ*, 648, L1  
 Ciardi B., Madau P., 2003, *ApJ*, 596, 1  
 Ciardi B., Ferrara A., Marri S., Raimondo G., 2001, *MNRAS*, 324, 381  
 Davis M., Efstathiou G., Frenk C. S., White S. D. M., 1985, *ApJ*, 292, 371  
 Dijkstra M., Haiman Z., Loeb A., 2004, *ApJ*, 613, 646  
 Elvis M., et al., 1994, *ApJS*, 95, 1  
 Gnedin N. Y., Abel T., 2001, *NewA*, 6, 437  
 Furlanetto S. R., Zaldarriaga M., Hernquist L., 2004, *ApJ*, 613, 1  
 Fan X., et al., 2006, *AJ*, 131, 1203  
 Ferrarese L., 2002, *ApJ*, 578, 90  
 Field G. B., 1958, *Proc I.R.E.*, 46, 240  
 Fukugita M., Kawasaki M., 1994, *MNRAS*, 269, 563  
 Furlanetto S. R., Loeb A., 2002, *ApJ*, 579, 1  
 Jelić V., et al., 2009, arXiv, arXiv:0907.5179  
 Jelić V., et al., 2008, *MNRAS*, 381  
 Kuhlen M., Madau P., 2005, *MNRAS*, 363, 1069  
 Laor A., Fiore F., Elvis M., Wilkes B. J., McDowell J. C., 1997, *ApJ*, 477, 93  
 Labropoulos P., et al., 2009, arXiv, arXiv:0901.3359  
 Laursen P., Razoumov A. O., Sommer-Larsen J., 2009, *ApJ*, 696, 853  
 Madau P., Meiksin A., Rees M. J., 1997, *ApJ*, 475, 429  
 Magorrian J., et al., 1998, *AJ*, 115, 2285  
 Mellema G., Iliev I. T., Alvarez M. A., Shapiro P. R., 2006, *NewA*, 11, 374  
 Mesinger A., 2009, arXiv, arXiv:0910.4161  
 Mesinger A., Furlanetto S., 2007, *ApJ*, 669, 663  
 Nakamoto T., Umemura M., Susa H., 2001, *MNRAS*, 321, 593

- Nusser A., 2005, MNRAS, 359, 183  
Nusser A., Silk J., 1993, ApJ, 411, L1  
Page L., et al., 2007, ApJS, 170, 335  
Pawlik A. H., Schaye J., 2008, arXiv, 802, arXiv:0802.1715  
Pierleoni M., Maselli A., Ciardi B., 2009, MNRAS, 393, 872  
Razoumov A. O., Cardall C. Y., 2005, MNRAS, 362, 1413  
Ricotti M., Ostriker J. P., 2004, MNRAS, 352, 547  
Rijkhorst E.-J., Plewa T., Dubey A., Mellema G., 2006, A&A, 452, 907  
Ritzerveld J., Icke V., Rijkhorst E.-J., 2003, astro, arXiv:astro-ph/0312301  
Santos M. G., Amblard A., Pritchard J., Trac H., Cen R., Cooray A., 2008, ApJ, 689, 1  
Sazonov S. Y., Ostriker J. P., Sunyaev R. A., 2004, MNRAS, 347, 144  
Schaerer D., 2002, A&A, 382, 28  
Seljak U., Zaldarriaga M., 1996, ApJ, 469, 437  
Shull J. M., van Steenberg M. E., 1985, ApJ, 298, 268  
Spergel D. N., et al., 2007, ApJS, 170, 377  
Springel V., 2005, MNRAS, 364, 1105  
Springel V., Hernquist L., 2003, MNRAS, 339, 312  
Susa H., 2006, PASJ, 58, 445  
Thomas R. M., et al., 2009, MNRAS, 393, 32  
Thomas R. M., Zaroubi S., 2008, MNRAS, 384, 1080  
Tasitsiomi A., 2006, ApJ, 645, 792  
Vanden Berk D. E., et al., 2001, AJ, 122, 549  
Vignali C., Brandt W. N., Schneider D. P., 2003, AJ, 125, 433  
Volonteri M., Lodato G., Natarajan P., 2008, MNRAS, 383, 1079  
Valdés M., Ferrara A., 2008, MNRAS, 387, L8  
Whalen D., Norman M. L., 2006, ApJS, 162, 281  
Wouthuysen S. A., 1952, AJ, 57, 31  
Wyithe J. S. B., Loeb A., 2004, ApJ, 610, 117  
Yoshida N., Sokasian A., Hernquist L., Springel V., 2003, ApJ, 598, 73  
Zahn O., Lidz A., McQuinn M., Dutta S., Hernquist L., Zaldarriaga M., Furlanetto S. R., 2007, ApJ, 654, 12  
Zaroubi S., Thomas R. M., Sugiyama N., Silk J., 2007, MNRAS, 375, 1269  
Zaroubi S., Silk J., 2005, MNRAS, 360, L64